Accepted Manuscript

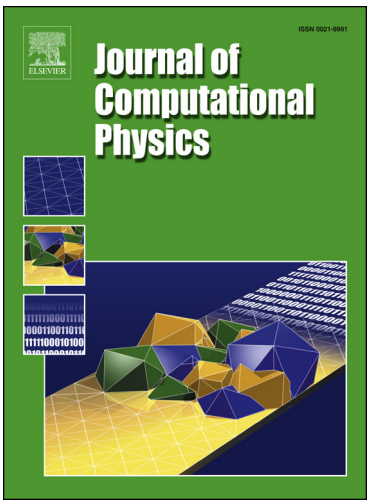

Paired explicit Runge-Kutta schemes for stiff systems of equations

Brian C. Vermeire

PII: S0021-9991(19)30339-0
DOI: https://doi.org/10.1016/j.jcp.2019.05.014
Reference: YJCPH 8687

To appear in: *Journal of Computational Physics*

Received date: 11 April 2018
Revised date: 14 March 2019
Accepted date: 7 May 2019

Please cite this article in press as: B.C. Vermeire, Paired explicit Runge-Kutta schemes for stiff systems of equations, *J. Comput. Phys.* (2019), https://doi.org/10.1016/j.jcp.2019.05.014

Highlights

- A new Paired Explicit Runge-Kutta (P-ERK) scheme is introduced.
- This approach allows different RK schemes to be used in stiff/non-stiff regions.
- P-ERK families are optimized and used for the Euler and Navier-Stokes equations.
- Results demonstrate up to 5x speedup relative to classical Runge-Kutta methods.

Paired Explicit Runge-Kutta Schemes for Stiff Systems of Equations

Brian C. Vermeire

Department of Mechanical, Industrial, and Aerospace Engineering
Concordia University
Montreal, QC, Canada

May 14, 2019

Abstract

In this paper we introduce a family of explicit Runge-Kutta methods, referred to as Paired Explicit Runge-Kutta (P-ERK) schemes, that are suitable for the solution of stiff systems of equations. The P-ERK approach allows Runge-Kutta schemes with a large number of derivative evaluations and large region of absolute stability to be used in the stiff parts of a domain, while schemes with relatively few derivative evaluations are used in non-stiff parts to reduce computational cost. Importantly, different P-ERK schemes with different numbers of derivative evaluations can be chosen based on local stiffness requirements and seamlessly paired with one another. We then verify that P-ERK schemes obtain their designed order of accuracy using the Euler equations with arbitrary combinations of schemes. We then demonstrate that P-ERK schemes can achieve speedup factors of approximately five for simulations using the Navier-Stokes equations including laminar and turbulent flow over an SD7003 airfoil. These results demonstrate that P-ERK schemes can significantly accelerate the solution of stiff systems of equations when using an explicit approach, and that they maintain accuracy with respect to conventional Runge-Kutta methods and available reference data.

1 Introduction

A wide-range of practical applications require the solution of locally-stiff systems of equations. For example, the convection-diffusion equation, reaction-diffusion equation, Navier-Stokes equations, Cahn-Hilliard equation, and the Euler equations at low Mach numbers or when resolving shocks, amongst others. The solution of such systems using an explicit approach, such as the popular explicit Runge-Kutta (RK) methods, often proves impractical [1, 2]. Numerical stiffness necessitates that prohibitively small time steps be taken to maintain stability, even if only a part of the computational domain is stiff [1, 3]. Implicit schemes are often used to overcome this limitation. However, this approach requires the storage and computationally expensive solution of a global system of linear or non-linear equations [1, 3]. Recent work on Implicit-Explicit (IMEX) RK schemes has shown particular promise using an implicit method for the stiff part of the domain and an explicit method for the non-stiff part [4, 5, 6, 7, 8]. However, this significantly increases the complexity of a solver and still requires the solution of a reduced local system of linear or non-linear equations. Hence, the solution of stiff systems of equations remains a particularly challenging problem in computational sciences and engineering [3]. While explicit methods have the disadvantage of being only conditionally stable, they also have several appealing properties. Explicit methods are often preferred due to their simplicity of implementation, scalability, and suitability for modern many-core hardware architectures. Hence, any approach that can alleviate the stability constraints of explicit methods would allow them to be applied to stiff systems of equations more efficiently, reducing the computational cost of solving such problems.

Previous research on the suitability of explicit RK methods for stiff systems of equations has focused on optimizing their region of absolute stability for increasingly large numbers of stages. For example, Allampalli et al. developed fourth-order high-accuracy large-step explicit Runge–Kutta (HALE-RK) schemes for computational aeroacoustics [9], Toulorge and Desmet created optimal explicit RK schemes for wave propagation problems [10], Diehl et al. studied low-storage methods for Maxwell's equations [11], Niegemann and Diehl created low-storage RK methods with optimized stability regions [12], Bernardini and Pirozzoli provided a strategy for optimizing schemes for wave propagation [13], Parsani et al. created optimal schemes for high-order discretizations of wave propagation problems [14], and Kubatko et al. optimized RK methods for discontinuous Galerkin (DG) spatial discretizations [15]. Furthermore, van Der Houwen and Sommeijer introduced large stage count explicit schemes with favourable internal stability properties [16] and Medovikov [17], Abdulle and Medovikov [18], Abdulle [19], and Abdulle and Vilmart [20] proposed explicit orthogonal Runge-Kutta Chebyshev (ROCK) methods for systems with large negative real eigenvalues, such as those encountered with parabolic systems, and a partitioned implicit–explicit orthogonal Runge–Kutta (PIROCK) method for advection-diffusion-reaction problems. Later, Martín-Vaquero and Janssen proposed explicit methods with up to 320 stages for parabolic problems [21], O'Sullivan introduced factorized Runge-Kutta-Chebyshev (FRKC) methods with large stage counts that are internally stable via a sequencing algorithm to limit internal amplification and Runge-Kutta-Gegenbauer schemes for mixed hyperbolic-parabolic problems [22, 23, 24], and Verwer et al. used Runge-Kutta-Chebyshev (RKC) schemes for advection-diffusion-reaction problems including extended imaginary stability regions for the advective part [25]. Hence, significant effort has been put into the optimization of Runge-Kutta stability polynomials and their efficient application to various systems of equations. Recently, it has been shown that the stability region of RK methods can be readily optimized for a large number of stages [26]. However, the computational efficiency advantage of each additional stage typically diminishes for large numbers of stages for advection dominated problems [15]. Another approach to adapt explicit RK methods for stiff systems of equations are multirate timestepping methods. These methods allow different schemes with different time step sizes to be used in different parts of the domain. For example, Constantinescu and Sandu introduced two second-order multirate methods [27], Seny et al. used multirate methods for geophysical flows [28], and Schlegel et al. introduced a recursive multirate scheme for advection equations [29]. However, the approaches of Constantinescu and Sandu [27] and Schlegel et al. [29] include only two different schemes being paired, they can require additional interface schemes, and the stability polynomials of these schemes are constrained by the underlying classical RK methods from which they are built.

Building on these previous studies, in this work we propose a general formulation for second-order schemes for the solution of locally-stiff systems of equations referred to as Paired Explicit Runge-Kutta (P-ERK) schemes. Although P-ERK schemes are similar to multirate schemes, their formulation is not based on an extension of classical methods using different time step sizes. Instead, they use a general formulation that describes families of schemes. These schemes are then chosen by optimizing their stability polynomials for a given spatial discretization. These new schemes have arbitrarily large numbers of stages and any number of schemes with the same number of stages but different stability polynomials can be paired. These P-ERK schemes can require significantly fewer derivative evaluations in the non-stiff parts of the domain compared to the stiff part, when contrasted against previous methods [27]. In the stiff parts a scheme with a large number of stage derivative evaluations and large region of absolute stability is used. In the non-stiff part, where stability constraints are not as prohibitive, a scheme with a small number of stage derivative evaluations is used to reduce computational cost. We will demonstrate that any number of these schemes can be paired together based on local stiffness criteria. We will then demonstrate the utility of P-ERK schemes when paired with high-order unstructured spatial discretizations. Finally, we explore their application to the Euler and Navier-Stokes equations, evaluating accuracy and performance relative to classical RK methods.

This manuscript is organized as follows. In Chapter 2 we introduce a general Butcher tableau for second-order P-ERK schemes with an arbitrary number of stages and derivative evaluations. In Chapter 3 we discuss the stability polynomial of these new families, and how they can be efficiently optimized for a given spatial discretization. In Chapter 4 we present an example application using optimal schemes for the high-order Flux Reconstruction approach constructed using von Neumann analysis techniques [30, 31]. In Chapter 5 we present verification of the approach and an assessment of performance for simulations using the Euler and Navier-Stokes equations. Finally, in Chapter 6 we present conclusions and topics for future work.

2 A New Family of Schemes

2.1 Background

A general RK method $\text{RK}_{s,e,p}$ having s-stages, of order p, and requiring e derivative evaluations, can be represented compactly in matrix-vector form using a Butcher tableau [3]

$$\begin{array}{c|c} \mathbf{c} & \mathbf{A} \\ \hline & \mathbf{b} \end{array} \tag{1}$$

where

$$\mathbf{A} = \begin{bmatrix} a_{1,1} & a_{1,2} & \dots & a_{1,s} \\ a_{2,1} & a_{2,2} & \dots & a_{2,s} \\ \vdots & \vdots & \ddots & \vdots \\ a_{s,1} & a_{s,2} & \dots & a_{s,s} \end{bmatrix}, \tag{2}$$

and

$$c_i = \sum_{j=1}^{s} a_{i,j}, \tag{3}$$

$$\sum_{i=1}^{s} b_i = 1. \tag{4}$$

For explicit schemes we also require

$$a_{i,j} = 0, \quad j \geq i, \tag{5}$$

which ensures $\mathbf{A}$ is strictly lower triangular. An explicit RK method can always be expressed as [2, 26]

$$u^{n+1} = P_{e,p}(z)u^n, \tag{6}$$

where $P_{e,p}(z)$ is the schemes stability polynomial, e is the number of derivatives evaluated, p is the order of accuracy, z is a point in the complex plane, u^n is the current solution at timestep n, and u^{n+1} is the solution at the next timestep. We are able to investigate the stability properties of an explicit RK scheme by taking $z = \omega\Delta t$, where ω is an eigenvalue of the system of equations being solved and Δt is the time step size. The resulting scheme will be linearly stable for this eigenvalue provided $|P_{e,p}(z)| \leq 1$, where $|\cdot|$ is the complex modulus. The stability polynomial of an explicit RK method can be determined directly from the Butcher tableau [1, 2]

$$P_{e,p}(z) = 1 + z\mathbf{b}^T \left(\mathbf{I} - z\mathbf{A}\right)^{-1} \mathbf{e}, \tag{7}$$

and via Cramer's rule [1, 2]

$$P_{e,p}(z) = \frac{\det\left(\mathbf{I} - z\mathbf{A} + z\mathbf{e}\mathbf{b}^T\right)}{\det\left(\mathbf{I} - z\mathbf{A}\right)}, \tag{8}$$

where $\mathbf{e}$ is a vector of ones. The region of absolute stability S of an explicit RK method is the set in the complex plane where this condition holds, that is [26],

$$S = \left\{ z \in \mathbb{C} : |P_{e,p}(z)| \leq 1 \right\}, \tag{9}$$

and the linear stability condition is

$$\Delta t\omega \subseteq S. \tag{10}$$

It is known that there exist no unconditionally stable explicit RK methods [2]. Hence, for a given spatial discretization there exists a maximum time-step size, denoted by Δt_{max}, beyond which an explicit RK discretization will become unstable. Due to this stability restriction, explicit methods often require a prohibitively large number of time-steps be taken when solving stiff systems of equations.

2.2 The Butcher Tableau

In this work we explore a new family of second-order P-ERK schemes. This family is designed such that different RK schemes with the same number of stages can be used for the stiff and non-stiff regions of a locally-stiff system of equations. In the non-stiff region a scheme with relatively few derivative evaluations is used to minimize computational cost. In the stiff regions a scheme with a large number of derivative evaluations is used. These additional derivatives are exploited to improve the region of absolute stability, allowing for a larger global time-step to be used. As will be shown, any number of schemes with the same number of stages from this family can be paired to conform to local stiffness requirements while reducing computational cost.

The Butcher tableau for a member of the new P-ERK$_{s,e,2}$ family is created starting from a general explicit RK scheme having the constraints [2]

$$a_{i,j} = 0, \quad j \geq i, \tag{11}$$

and correspondingly

$$c_1 = 0. \tag{12}$$

This gives the following Butcher tableau

$$\begin{array}{c|c} \mathbf{c} & \mathbf{A} \\ \hline & \mathbf{b} \end{array} = \begin{array}{c|cccccc} 0 & 0 & & & & & \\ c_2 & a_{2,1} & 0 & & & & \\ c_3 & a_{3,1} & a_{3,2} & 0 & & & \\ c_4 & a_{4,1} & a_{4,2} & a_{4,3} & \ddots & & \\ \vdots & \vdots & \vdots & \vdots & \ddots & 0 & \\ c_s & a_{s,1} & a_{s,2} & a_{s,3} & \dots & a_{s,s-1} & 0 \\ \hline & b_1 & b_2 & b_3 & \dots & b_{s-1} & b_s \end{array} \tag{13}$$

One disadvantage of such a scheme is that it requires a large amount of memory to store s stage derivatives. To avoid increasing memory consumption relative to conventional Runge-Kutta methods we can alleviate storage requirements by setting

$$a_{i,j} = 0, \quad j > 1, \quad i > j + 1, \tag{14}$$

$$b_i = 0, \quad i < s, \tag{15}$$

$$b_s = 1. \tag{16}$$

This yields the following general Butcher tableau

$$\begin{array}{c|c} \mathbf{c} & \mathbf{A} \\ \hline & \mathbf{b} \end{array} = \begin{array}{c|cccccc} 0 & 0 & & & & & \\ c_2 & a_{2,1} & 0 & & & & \\ c_3 & a_{3,1} & a_{3,2} & 0 & & & \\ c_4 & a_{4,1} & 0 & a_{4,3} & \ddots & & \\ \vdots & \vdots & \vdots & \vdots & \ddots & 0 & \\ c_s & a_{s,1} & 0 & 0 & \dots & a_{s,s-1} & 0 \\ \hline & 0 & 0 & 0 & \dots & 0 & b_s \end{array} \tag{17}$$

This tableau has the unique property that it requires only two stage derivatives be stored simultaneously, regardless of the total number of stages. This greatly reduces memory requirements. Furthermore, such a scheme will be second-order accurate provided [2]

$$c_s = \frac{1}{2}. \tag{18}$$

We then choose the remaining $\mathbf{c}$ coefficients to be equidistant between the first and last stages

$$c_i = \frac{i-1}{2(s-1)}, \tag{19}$$

noting that these could be optimized in future studies to improve some non-linear properties of the scheme, for example, its Strong Stability Preserving (SSP) behaviour. Also, noting that

$$c_i = \sum_{j=1}^{s} a_{i,j}, \tag{20}$$

the general tableau simplifies to just one unknown $a_{i,j}$ value per stage

$$\begin{array}{c|c} \mathbf{c} & \mathbf{A} \\ \hline & \mathbf{b} \end{array} = \begin{array}{c|cccccc} 0 & 0 & & & & & \\ c_2 & a_{2,1} & 0 & & & & \\ c_3 & c_3 - a_{3,2} & a_{3,2} & 0 & & & \\ c_4 & c_4 - a_{4,3} & 0 & a_{4,3} & \ddots & & \\ \vdots & \vdots & \vdots & \vdots & \ddots & 0 & \\ c_s & c_s - a_{s,s-1} & 0 & 0 & \dots & a_{s,s-1} & 0 \\ \hline & 0 & 0 & 0 & \dots & 0 & b_s \end{array} \tag{21}$$

where each c_i is known explicitly through Equation (20). Hence, for every additional stage we add to such a tableau, we add one additional unknown stage coefficient. Finally, to reduce the number of stage derivative evaluations to e for a general P-ERK$_{s,e,2}$ scheme we set

$$a_{i+1,i} = 0, \quad 2 \leq i \leq s - e + 1, \tag{22}$$

which gives a scheme that has $e-2$ unknown Butcher tableau coefficients. Following this approach, an example Butcher tableau for a P-ERK$_{10,6,2}$ scheme is

$$\begin{array}{c|c} \mathbf{c} & \mathbf{A} \\ \hline & \mathbf{b} \end{array} = \begin{array}{c|cccccccccc} 0 & 0 & 0 & 0 & 0 & 0 & 0 & 0 & 0 & 0 & 0 \\ \frac{1}{18} & \frac{1}{18} & 0 & 0 & 0 & 0 & 0 & 0 & 0 & 0 & 0 \\ \frac{1}{9} & \frac{1}{9} & 0 & 0 & 0 & 0 & 0 & 0 & 0 & 0 & 0 \\ \frac{1}{6} & \frac{1}{6} & 0 & 0 & 0 & 0 & 0 & 0 & 0 & 0 & 0 \\ \frac{2}{9} & \frac{2}{9} & 0 & 0 & 0 & 0 & 0 & 0 & 0 & 0 & 0 \\ \frac{5}{18} & \frac{5}{18} & 0 & 0 & 0 & 0 & 0 & 0 & 0 & 0 & 0 \\ \frac{1}{2} & \frac{1}{2} - a_{7,6} & 0 & 0 & 0 & 0 & a_{7,6} & 0 & 0 & 0 & 0 \\ \frac{7}{18} & \frac{7}{18} - a_{8,7} & 0 & 0 & 0 & 0 & 0 & a_{8,7} & 0 & 0 & 0 \\ \frac{4}{9} & \frac{4}{9} - a_{9,8} & 0 & 0 & 0 & 0 & 0 & 0 & a_{9,8} & 0 & 0 \\ \frac{1}{2} & \frac{1}{2} - a_{10,9} & 0 & 0 & 0 & 0 & 0 & 0 & 0 & a_{10,9} & 0 \\ \hline & 0 & 0 & 0 & 0 & 0 & 0 & 0 & 0 & 0 & 1 \end{array} \tag{23}$$

and its corresponding stability polynomial determined from Equation (8) is

$$P_{6,2}(z) = 1 + z + \frac{z^2}{2} + \frac{4a_{10,9}z^3}{9} + \frac{7a_{9,8}a_{10,9}z^4}{18} + \frac{a_{8,7}a_{9,8}a_{10,9}z^5}{3} + \frac{5a_{7,6}a_{8,7}a_{9,8}a_{10,9}z^6}{18}. \tag{24}$$

Hence, when provided any suitable stability polynomial $P_{e,2}$ we can determine the unknown P-ERK$_{s,e,2}$ Butcher tableau coefficients via the general form of the schemes stability polynomial.

To summarize, we have created a general family of second-order P-ERK schemes that have s stages and require e derivative evaluations. Importantly, we note that all such schemes having the same number of stages share a common $\mathbf{b}$ and $\mathbf{c}$. Hence, they can be paired in a similar manner to the IMEX approach [4]. This allows P-ERK schemes with different numbers of derivative evaluations and terms in their stability polynomials to be used in different parts of the domain. Finally, a unique scheme can be determined by providing a suitable stability polynomial for the system of equations to be solved.

3 The Stability Polynomial

In the previous section we introduced the second-order P-ERK$_{s,e,2}$ family of schemes that have $e-2$ unknown entries in their Butcher tableau and the same $e-2$ unknown terms in their stability polynomials. Hence, given a suitable stability polynomial we can solve for the $e-2$ unknown $a_{i,j}$ coefficients directly, which then completes the Butcher tableau. While it is possible to use existing stability polynomials, it is often desirable to optimize the stability polynomial for a given spatial discretization to allow large time steps to be taken. The stability polynomial $P_{e,p}(z)$ of an e derivative evaluation order p explicit RK method is a polynomial of degree e defined by monomial coefficients γ_j according to [26]

$$P_{e,p}(z) = \sum_{j=0}^{e} \gamma_j z^j. \tag{25}$$

To be accurate to order p we require the stability polynomial coefficients to be the exponential function up to terms of at least order p, that is

$$\gamma_j = \frac{1}{j!} \ \ for \ 0 \le j \le p. \tag{26}$$

In the current study we only consider second-order P-ERK$_{s,e,2}$ schemes. Applying the order of accuracy constraints to the stability polynomial we obtain

$$P_{e,2}(z) = 1 + z + \frac{z^2}{2} + \sum_{j=3}^{e} \gamma_j z^j, \tag{27}$$

which has $e-2$ free parameters $\{\gamma_3, \ldots, \gamma_e\}$.

For any explicit scheme we can determine the largest time-step Δt_{max} for which the stability constraint of Equation (10) remains satisfied. Our objective is to determine the set of free parameters $\{\gamma_3, \ldots, \gamma_e\}$ that yield the largest possible value of Δt_{max} for a given spatial discretization. This can be cast as an optimization problem to [26]

$$\begin{aligned} &\underset{\gamma_3,\ldots,\gamma_e}{\text{maximize}} \quad \Delta t \\ &\text{subject to} \quad |P_{e,2}(\Delta t \omega^\delta)| - 1 \leq 0, \quad \forall \omega^\delta, \end{aligned} \tag{28}$$

where ω^δ is one from the set of all possible eigenvalues $\boldsymbol{\omega}^\delta$. We use Δt_{opt} to denote the optimized value of the maximum stable time step size Δt_{max}, and P_{opt} to denote the corresponding optimal stability polynomial. Finding the global optimum in Equation (30) can be particularly challenging as it is nonconvex for $e > 2$ and there are typically several sub-optimal local minima [26].

Ketcheson and Ahmadia [26] proposed an alternate optimization approach, which seeks to first determine how small the maximum modulus of $P_{e,p}(\Delta t \omega^\delta)$ can be for a given Δt, which can be cast as trying to

$$\underset{\gamma_{p+1},\gamma_{p+2},\ldots,\gamma_e}{\text{minimize}} \quad \underset{\omega^\delta \in \boldsymbol{\omega}^\delta}{max} \left(|P_{e,p}(\Delta t \omega^\delta)| - 1 \right). \tag{29}$$

The solution to Equation (29) is denoted $r_{e,p}(\Delta t, \boldsymbol{\omega}^\delta)$ and we note that $|P_{e,p}(z)|$ is linear in γ_j. Therefore, Equation (29) is convex [26]. Ketcheson and Ahmadia [26] then reformulated the problem in Equation (30) as

$$\begin{aligned} &\underset{\gamma_{p+1},\gamma_{p+2},\ldots,\gamma_e}{\text{maximize}} \quad \Delta t \\ &\text{subject to} \quad r_{e,p}(\Delta t, \boldsymbol{\omega}^\delta) \leq 0. \end{aligned} \tag{30}$$

This is an optimization problem in a single variable, and can be handled by the simple bisection method outlined in Algorithm 1. The solution of Algorithm 1 yields the maximum possible linearly stable time-step Δt_{opt}, as well as the corresponding optimal stability polynomial P_{opt}.

Algorithm 1: Finding Δt_{opt}.

Select Δt_{max}
$\Delta t_{min} = 0$
while $\Delta t_{max} - \Delta t_{min} > \epsilon$ **do**
  $\Delta t = \frac{\Delta t_{min} + \Delta t_{max}}{2}$
  Solve Equation (29)
  if $r_{e,s}(\Delta t, \boldsymbol{\omega}^\delta) \leq 0$ **then**
    $\Delta t_{min} = \Delta t$
  else
    $\Delta t_{max} = \Delta t$
  end
end
return $\Delta t_{opt} = \Delta t_{min}$

In the current study we converge the bisection method in Algorithm 2 to 10^{-12} using Matlab 2016a [32]. To solve the convex minimization problem in Equation (29) we used CVX, which is a Matlab-based package for specifying and solving convex programs, using the "best" precision setting [33, 34]. Following this approach we can generate an optimal stability polynomial for a given system of equations, which uniquely determines the Butcher tableau.

4 Application to High-Order Unstructured Methods

One particularly appealing application of P-ERK schemes is the solution of stiff systems of equations using high-order unstructured spatial discretizations, such as Discontinuous Galerkin (DG) [35, 36], Spectral

Difference (SD) [37, 38], and Flux Reconstruction (FR) [30, 31]. These schemes use an element-wise degree k polynomial representation of the solution and typically achieve an order of accuracy of $k + 1$. They are also suitable for complex geometries utilizing mixed-element unstructured meshes. However, it is well known that higher-order variants of these schemes have stricter stability constraints per degree of freedom than conventional lower-order Finite Volume (FV) or Finite Difference (FD) methods [30]. Hence, they typically require small time-steps to maintain stability. In this section we focus on the FR approach, since it can recover both DG and SD methods [30]. Our objective is to demonstrate that we can generate semi-discrete eigenspectra $\boldsymbol{\omega}^\delta$ via Von Neumann analysis for advection dominated problems using the FR approach. These eigenspectra can then be used to generate optimal stability polynomials for various numbers of derivative evaluations and solution polynomial degrees, which in turn can be used to generate corresponding P-ERK schemes.

4.1 Flux Reconstruction

The FR approach, first introduced by Huynh [30], later described using our notation in [39, 40, 41] and included here for completeness, is used to spatially discretize a 1D hyperbolic conservation law of the form

$$\frac{\partial u}{\partial t} + \frac{\partial f}{\partial x} = 0, \tag{31}$$

in a domain $\mathbf{\Omega}$, where $u = u(x, t)$ is the solution with a given initial distribution $u(x, 0) = u_0$, t is time, $f = f(u)$ is the flux, and x is the spatial coordinate.

We start by splitting the domain $\mathbf{\Omega}$ into a mesh composed of elements

$$\mathbf{\Omega} = \bigcup_{n=1}^{N_e} \mathbf{\Omega}_n, \qquad \bigcap_{n=1}^{N_e} \mathbf{\Omega}_n = \emptyset, \tag{32}$$

where $\mathbf{\Omega}_n$ is one of N_e elements in the domain. For simplicity, each element $\mathbf{\Omega}_n$ is mapped to a reference element I via the linear mapping

$$\xi = \Gamma_n(x) = 2\left(\frac{x - x_n}{x_{n+1} - x_n}\right) - 1, \tag{33}$$

where x_n is the mesh node corresponding to the left face of $\mathbf{\Omega}_n$, Γ_n is the mapping function, and ξ is the location in reference space. This mapping can be inverted according to

$$x = \Gamma_n^{-1}(\xi) = \left(\frac{1 - \xi}{2}\right) x_n + \left(\frac{1 + \xi}{2}\right) x_{n+1}, \tag{34}$$

which is also linear. This allows us to construct the transformed solution in computational space according to

$$\hat{u}_n^\delta = \hat{u}_n^\delta(\xi, t) = u_n^\delta\left(\Gamma_n^{-1}(\xi), t\right), \tag{35}$$

and a transformed flux in computational space according to

$$\hat{f}_n^\delta = \hat{f}_n^\delta(\xi, t) = \frac{f_n^\delta\left(\Gamma_n^{-1}(\xi), t\right)}{h_n}. \tag{36}$$

The system of equations in computational space can then be written as

$$\frac{\partial \hat{u}_n^\delta}{\partial t} + \frac{\partial \hat{f}_n^\delta}{\partial \xi} = 0. \tag{37}$$

Following Huynh [30], the solution within each element is represented by a degree k polynomial, which is allowed to be discontinuous at the interface between elements. This polynomial is supported by

nodal basis functions generated at $k+1$ solution points. Therefore, the solution within each element in computational space can be approximated as

$$\hat{u}_n^\delta = \sum_{l=0}^{k} \hat{u}_{n,l}^\delta \hat{\phi}_l, \tag{38}$$

where $\hat{u}_n^\delta = \hat{u}_n^\delta(\xi, t)$ is the polynomial representation of the solution within an element, $\hat{u}_{n,l}^\delta = \hat{u}_{n,l}^\delta(t)$ is the value of the solution at solution point l, and $\hat{\phi}_l = \hat{\phi}_l(\xi)$ is its corresponding nodal basis function in reference space. For the one-dimensional case these basis functions are the Lagrange polynomials

$$\hat{\phi}_l(\xi) = \prod_{m=0, m\neq l}^{k} \frac{\xi - \xi_m}{\xi_l - \xi_m}. \tag{39}$$

A polynomial representation of the discontinuous flux function $\hat{f}_n^{\delta D} = \hat{f}_n^{\delta D}(x, t)$ can be constructed using the same polynomial basis as the solution according to

$$\hat{f}_n^{\delta D} = \sum_{l=0}^{k} \hat{f}_{n,l}^\delta \hat{\phi}_l, \tag{40}$$

where the superscript D denotes that this flux, like the solution, is allowed to be discontinuous at the interface between elements and $\hat{f}_{n,l}^\delta = \hat{f}_{n,l}^\delta(t)$ is the flux evaluated at the solution points. This discontinuous flux is then corrected to be C_0 continuous by

$$\hat{f}_n^{\delta C} = \left(\hat{f}_n^{CL} - \hat{f}_{n,L}^{\delta D}\right) g_L + \left(\hat{f}_n^{CR} - \hat{f}_{n,R}^{\delta D}\right) g_R, \tag{41}$$

where $g_L = g_L(\xi)$ and $g_R = g_R(\xi)$ are correction functions, $\hat{f}_{n,L}^{\delta D} = \hat{f}_n^{\delta D}(-1, t)$, and $\hat{f}_{n,R}^{\delta D} = \hat{f}_n^{\delta D}(1, t)$. The terms $\hat{f}_n^{CL} = \hat{f}_n^{CL}(u_L^-, u_L^+)$ and $\hat{f}_n^{CR} = \hat{f}_n^{CR}(u_R^-, u_R^+)$ are common interface fluxes computed at the flux points between elements by an appropriate Riemann solver using the interpolated values u_L^-, u_L^+, u_R^-, and u_R^+ of the solution from the adjoining elements at the left (L) and right (R) interfaces. The correction functions are degree $k+1$ polynomials with the constraints

$$g_L(-1) = 1, \qquad g_L(1) = 0, \tag{42}$$

$$g_R(-1) = 0, \qquad g_R(1) = 1. \tag{43}$$

The gradient of the continuous flux function can then be found according to

$$\frac{\partial \hat{f}_n^\delta}{\partial \xi} = \frac{\partial \hat{f}_n^{\delta D}}{\partial \xi} + \frac{\partial \hat{f}_n^{\delta C}}{\partial \xi} = \sum_{l=0}^{k} \hat{f}_{n,l}^\delta \frac{\partial \hat{\phi}_l}{\partial \xi} + \left(\hat{f}_n^{CL} - \hat{f}_{n,L}^{\delta D}\right) \frac{\partial g_L}{\partial \xi} + \left(\hat{f}_n^{CR} - \hat{f}_{n,R}^{\delta D}\right) \frac{\partial g_R}{\partial \xi}, \tag{44}$$

which is of degree k and in the same polynomial space as $\hat{u}_n^\delta$.

The behaviour of an FR scheme depends on the choice of correction functions g_L and g_R for the left and right hand boundaries, respectively. Huynh [30] originally introduced several correction functions including one that recovered a collocation-based nodal DG scheme, one that recovered an energy-stable SD scheme, and one that recovered a so-called g_2 scheme. Vincent et al. [39, 42] later introduced a single-parameter family of energy-stable flux reconstruction schemes, whose semi-discrete dispersion and dissipation behaviour has previously been studied.

4.2 Von Neumann Analysis

To determine the stability constraints of an FR scheme we perform Von Neumann analysis following Huynh [30], Vincent et al [39], and Vermeire et al. [40, 41]. A full description of the approach is included here for completeness. For this study, we consider the linear advection equation with fully upwind fluxes

at element interfaces, which has similar behaviour to multidimensional advection dominated problems using the Euler and Navier-Stokes equations.

We follow the notation of Vincent et al. [39] for Von Neumann analysis of a general linear advection equation

$$\frac{\partial u}{\partial t} + \frac{\partial u}{\partial x} = 0, \tag{45}$$

which admits plane wave solutions of the form

$$u = e^{I(\theta x - \omega t)}, \tag{46}$$

provided the temporal frequency $\omega = \omega(\theta)$ satisfies the dispersion relation where θ is the wave number and $I = \sqrt{-1}$. Specifically, we consider a mesh where all elements have constant width $h = 1$. The flux reconstruction scheme can then be cast in matrix-vector form for any element as

$$\frac{\partial \hat{\mathbf{u}}^{\delta}}{\partial t} = -2\mathbf{D}\hat{\mathbf{u}}^{\delta} - \left(\hat{f}^{CL} - 2\mathbf{l}^{T}\hat{\mathbf{u}}^{\delta}\right)\mathbf{g}_{\xi L}, \tag{47}$$

where $\hat{\mathbf{u}}^{\delta}$ is the vector of solution point values, $\mathbf{g}_{\xi L}$ is the gradient of the correction function evaluated at the solution points,

$$\mathbf{l}[k] = \hat{\phi}_{j,k}(-1), \tag{48}$$

is the boundary extrapolation operator, and $\mathbf{D}$ is the nodal gradient operator.

We seek Bloch wave type solution to Equation (47) of the form

$$\hat{\mathbf{u}}^{\delta} = e^{I\left(n\overline{\theta}^{\delta} - \omega^{\delta} t\right)}\hat{\mathbf{v}}^{\delta}, \tag{49}$$

where $\overline{\theta}^{\delta}$ is a prescribed baseline wavenumber within the range $-\pi \leq \overline{\theta} \leq \pi$ and ω^{δ} is the resulting temporal frequency of the scheme. The upwind interface flux can then be written as

$$\hat{f}^{CL} = 2\mathbf{r}^{T} e^{I\left(n\overline{\theta}^{\delta} - \overline{\theta}^{\delta} - \omega^{\delta} t\right)}\hat{\mathbf{v}}^{\delta}, \tag{50}$$

where

$$\mathbf{r}[l] = \hat{\phi}_{n,l}(1). \tag{51}$$

By substituting Equation (49) and Equation (50) into Equation (47) we obtain

$$\mathbf{Q}\hat{\mathbf{v}}^{\delta} = \omega^{\delta}\hat{\mathbf{v}}^{\delta}, \tag{52}$$

where

$$\mathbf{Q} = -2I\left[\mathbf{D} + \mathbf{g}_{\xi L}\left(\mathbf{r}^{T} e^{-I\overline{\theta}^{\delta}} - \mathbf{l}^{T}\right)\right]. \tag{53}$$

Equation (52) is a classical eigenvalue problem, where $\hat{\mathbf{v}}$ is one of $k + 1$ valid eigenvectors with an associated eigenvalue ω^{δ}. The operator $\mathbf{Q}$ is a function of $\overline{\theta}^{\delta}$, and it follows that so too are $\hat{\mathbf{v}}^{\delta}$ and ω^{δ}. In order for a fully discrete scheme to remain stable, all of the eigenvalues ω^{δ} from the spatial discretization must be contained within the region of absolute stability of the temporal discretization for all permissible values of $\overline{\theta}^{\delta}$ for a given Δt. Example semi-discrete eigenspectra for solution polynomials of degree $k = 1$ to $k = 8$ are shown in Figure 1. The increasing spectral radius in these results demonstrates increasing numerical stiffness as the degree of the solution polynomial is increased when using the FR approach.

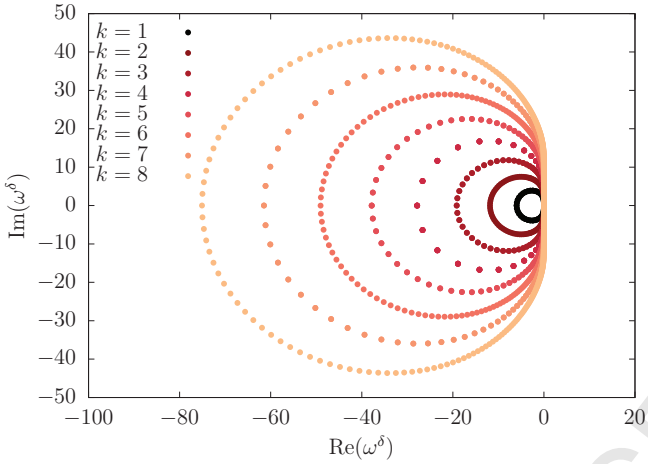

Figure 1. Example eigenspectra for the FR approach with the DG correction function and solution polynomials of degree $k = 1$ to $k = 8$.

4.3 Optimal Stability Polynomials

Using Equation (52) we can generate semi-discrete eigenspectra for the FR approach using a degree k scheme. These eigenspectra can then be used in Algorithm 1 to generate optimal stability polynomials. Using these optimal stability polynomials, we can then solve for the unknown Butcher tableau coefficients of a P-ERK scheme. A plot of Δt_{opt} for to $e = 2$ to $e = 16$ derivative evaluations is shown in Figure 2, and contours of an optimal stability polynomial and eigenspectra scaled by Δt_{opt} for $k = 6$ and $e = 16$ are shown in Figure 3. These results demonstrate that adding additional derivative evaluations and terms to the stability polynomial consistently increases the allowable time step size, that this increase in approximately linear for large numbers of stages, and that this procedure creates a stability polynomial that approximates the shape of the semi discrete eigenspectra when scaled by Δt_{opt}. Also, we see that even with their corresponding optimal stability polynomials, the higher-order FR discretizations remain stiffer than their lower-order variants with smaller values of Δt_{opt}. Finally, since the $P_{2,2}$ stability polynomial has no free parameters to be optimized, its performance in terms of Δt_{opt} for the higher-order schemes is poor. Hence, we have demonstrated that we can generate optimal stability polynomials for FR discretizations using Algorithm 1. These stability polynomials can then be used to directly generate Butcher tableaus for families of P-ERK$_{s,e,2}$ schemes. For example, the optimal stability polynomial for $k = 6$ and $e = 6$ is

$$P_{opt} = 1 + z + \frac{z^2}{2} + 0.1540265893599148z^3 + 0.0287139292526216z^4 + 0.0030119509086084z^5 + 0.0001374933831987z^6. \tag{54}$$

Comparing this with the general P-ERK$_{10,6,2}$ stability polynomial provided in Equation (24), we can directly solve for the unknown Butcher tableau coefficients using Equation (24), generating the P-ERK$_{10,6,2}$ scheme that has been optimized for a solution polynomial of degree $k = 6$. Optimal stability polynomials, values of Δt_{opt}, and complete Butcher tableaus are provided for solution polynomials of degree $k = 1$ to $k = 8$ and P-ERK schemes of up to 16 stages are provided as Electronic Supplementary Material with this manuscript.

5 Numerical Results

5.1 Isentropic Vortex Advection

For verification of P-ERK schemes we consider the propagation of an isentropic vortex through a periodic domain using the Euler equations. While not significantly stiff, this problem has an exact analytical

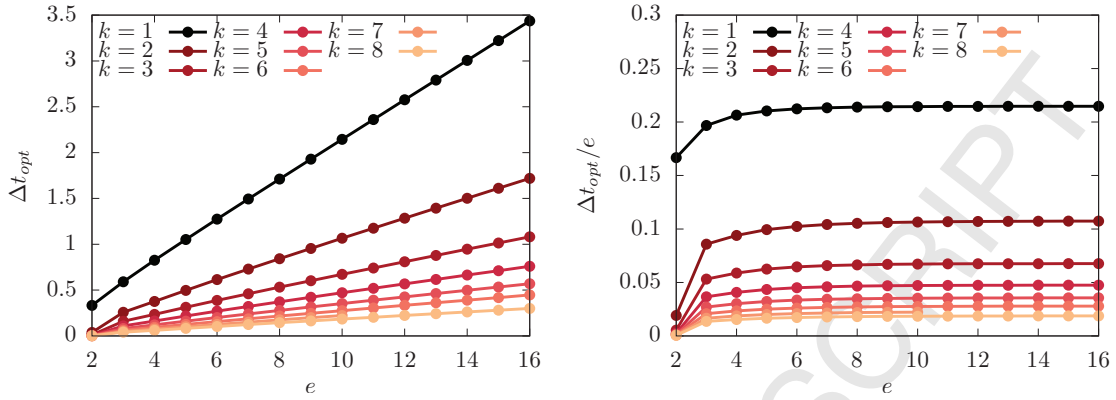

(a) Values of Δt_{opt}.

(b) Values of Δt_{opt} normalized by e.

Figure 2. Values of Δt_{opt} for solution polynomials of degree $k = 1$ to $k = 8$ with between $e = 2$ and $e = 16$ derivative evaluations.

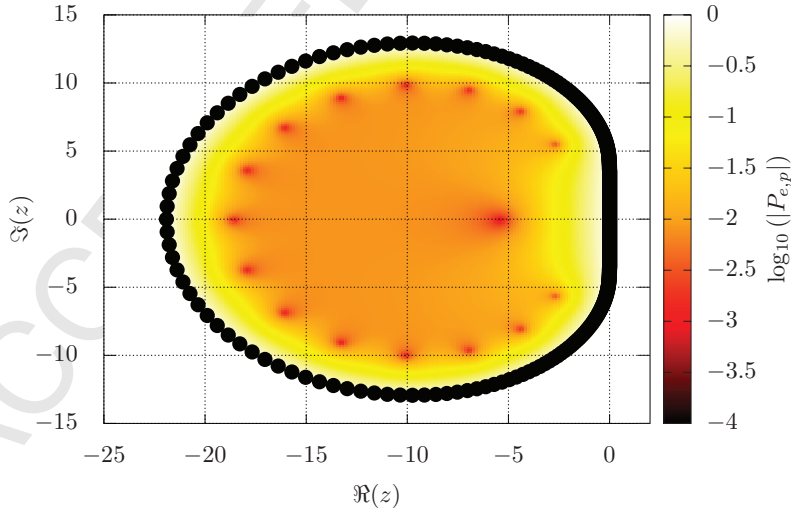

Figure 3. Contours of the optimal $P_{16,2}$ stability polynomial for solution polynomial of degree $k = 6$ including the spatial discretization eigenvalues scaled by their corresponding Δt_{max} (black circles).

solution making it useful for verification purposes. This exact solution is simply the propagation of the initial isentropic vortex with the mean flow. The initial flow field is specified as [43, 44]

$$\begin{aligned} \rho &= \left[1 - \frac{S^2 M^2 (\gamma - 1) e^{2f}}{8\pi^2}\right]^{\frac{1}{\gamma - 1}}, \\ u &= \frac{S y e^f}{2\pi R}, \\ v &= 1 - \frac{S x e^f}{2\pi R}, \\ p &= \frac{\rho^\gamma}{\gamma M^2}, \end{aligned} \tag{55}$$

where ρ is the density, u and v are the velocity components, p is the pressure, $f = (1 - x^2 - y^2)/2R^2$, $S = 13.5$ is the strength of the vortex, $M = 0.4$ is the free-stream Mach number, $R = 1.5$ is the characteristic vortex radius, and $\gamma = 1.4$. A plot of the initial density distribution is shown in Figure 4a.

We used a 20×20 two-dimensional domain with periodic boundary conditions on all four edges. The mesh was composed of 80×80 quadrilateral elements and the solution was represented using $k = 6$ degree polynomials on each element to minimize spatial error. The solution and flux points were located at Gauss points and Rusanov fluxes were used at the interfaces between elements. We run one set of simulations for the classical $\text{RK}_{2,2}$ scheme, one for each of the $\text{P-ERK}_{10,2,2}$ through $\text{P-ERK}_{10,10,2}$ schemes optimized for $k = 6$, as well as an additional simulation using a random distribution of these P-ERK schemes in the domain as shown in Figure 4b. Each simulation was run to a final time of $t = 20$ using four different time step sizes for a total of 44 simulations. To evaluate the accuracy of each scheme we considered the L_2 norm of the density error at the end of each simulation in a 4×4 region at the center of the domain. This L_2 error is defined as

$$\sigma = \sqrt{\int_{-2}^{2} \int_{-2}^{2} (\rho_\delta(\mathbf{x}) - \rho_e(\mathbf{x}))^2 \, d\mathbf{x}}, \tag{56}$$

where $\rho_\delta(\mathbf{x})$ is the final numerical solution and $\rho_e(\mathbf{x})$ is the exact analytical solution, which is identical to the initial condition. To get a good approximation of the true L_2 error we used a fifteenth-order quadrature rule within each element.

A summary of the density error for each temporal scheme and time step size including observed orders of accuracy are provided in Table 1 and plotted in Figure 5. We observe that all schemes achieve their designed order of accuracy of two, that schemes with more derivative evaluations have lower error for a given time step size, and that these schemes still have a small accuracy advantage when compared per derivative evaluation. Importantly, the simulation using a random distribution of $\text{P-ERK}_{10,e,2}$ schemes also achieves second-order accuracy with an intermediate level of error between that of the different schemes used. These results demonstrate that the $\text{P-ERK}_{s,e,2}$ families of schemes are able to achieve their designed order of accuracy for non-linear systems of equations, either on their own or paired together in arbitrary configurations. Hence, we have demonstrated that we are able to maintain accuracy while using different $\text{P-ERK}_{s,e,2}$ schemes in different parts of the domain.

5.2 Laminar SD7003 Airfoil

To evaluate the performance and accuracy of P-ERK schemes for the unsteady Navier-Stokes equations we consider laminar flow over an SD7003 airfoil. We use a freestream Mach number of $M = 0.2$ where $M = U_\infty / c_\infty$ where U_∞ and c_∞ are the freestream velocity and speed of sound, respectively. We use an angle of attack $\alpha = 4°$, ratio of specific heats $\gamma = 1.4$, Prandtl number $Pr = 0.71$, and Reynolds number $Re_c = 10,000$ where $Re_c = \rho_\infty U_\infty c / \mu$, c is the airfoil chord length, and μ is the constant viscosity. This is a commonly used test case for the verification and validation of CFD solvers. Reference results are available from Uranga et al. [45] using a high-order DG scheme and Lopez et al. [46] using the FR approach. At this Reynolds number and angle of attack the flow is expected to be planar with little

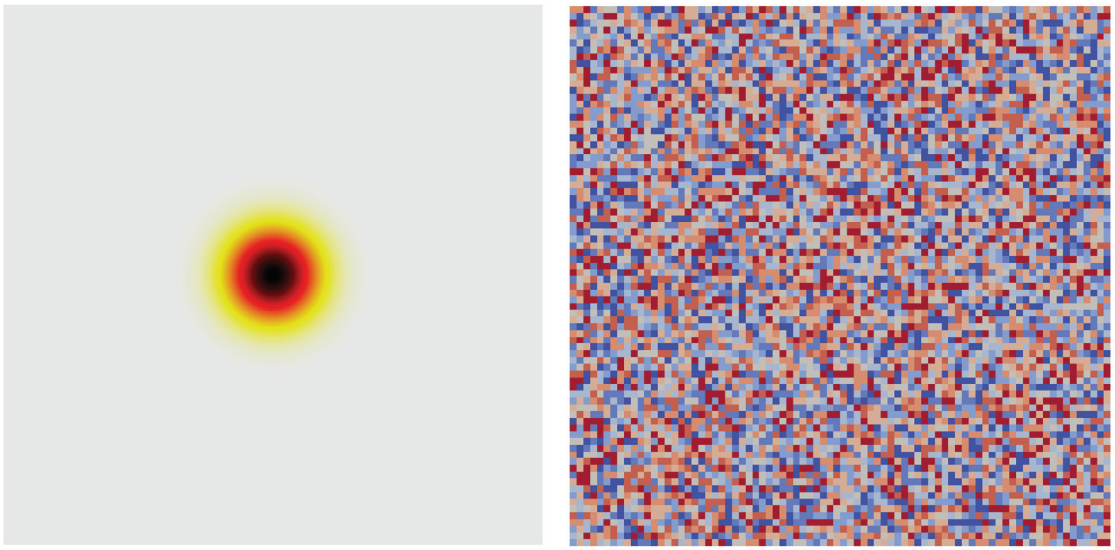

(a) Initial density distribution.

(b) Random P-ERK$_{10,e,2}$ distribution.

Figure 4. Initial density distribution, mesh, and random distribution of the P-ERK$_{10,e,2}$ schemes for $e = 2$ (blue) to $e = 10$ (red) for the isentropic vortex advection test case.

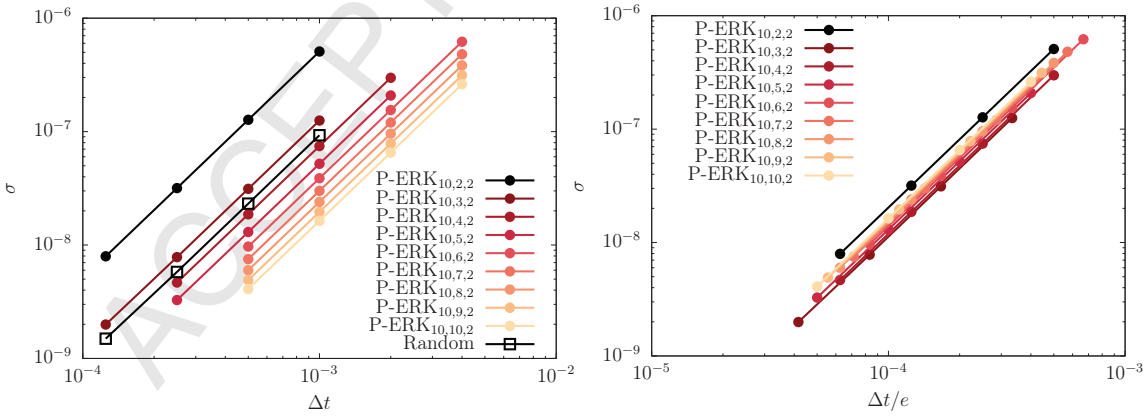

(a) Error vs. Δt.

(b) Error vs. Δt normalized by e.

Figure 5. Convergence plots for the isentropic vortex test case.

Table 1. Summary of density error and order of accuracy for the isentropic vortex test case using P-ERK optimized for the solution polynomial of degree $k = 6$.

Scheme	Δt	σ	*Order*
$RK_{2,2}$	1.00×10^{-3}	5.08×10^{-7}	
	5.00×10^{-4}	1.27×10^{-7}	2.00
	2.50×10^{-4}	3.17×10^{-8}	2.00
	1.25×10^{-4}	7.94×10^{-9}	2.00
$P\text{-}ERK_{10,2,2}$	1.00×10^{-3}	5.08×10^{-7}	
	5.00×10^{-4}	1.27×10^{-7}	2.00
	2.50×10^{-4}	3.17×10^{-8}	2.00
	1.25×10^{-4}	7.94×10^{-9}	2.00
$P\text{-}ERK_{10,3,2}$	1.00×10^{-3}	1.25×10^{-7}	
	5.00×10^{-4}	3.12×10^{-8}	2.00
	2.50×10^{-4}	7.82×10^{-9}	2.00
	1.25×10^{-4}	1.98×10^{-9}	1.98
$P\text{-}ERK_{10,4,2}$	2.00×10^{-3}	2.98×10^{-7}	
	1.00×10^{-3}	7.45×10^{-8}	2.00
	5.00×10^{-4}	1.86×10^{-8}	2.00
	2.50×10^{-4}	4.67×10^{-9}	2.00
$P\text{-}ERK_{10,5,2}$	2.00×10^{-3}	2.08×10^{-7}	
	1.00×10^{-3}	5.20×10^{-8}	2.00
	5.00×10^{-4}	1.30×10^{-8}	2.00
	2.50×10^{-4}	3.27×10^{-9}	2.00
$P\text{-}ERK_{10,6,2}$	4.00×10^{-3}	6.20×10^{-7}	
	2.00×10^{-3}	1.55×10^{-7}	2.00
	1.00×10^{-3}	3.87×10^{-8}	2.00
	5.00×10^{-4}	9.69×10^{-9}	2.00
$P\text{-}ERK_{10,7,2}$	4.00×10^{-3}	4.80×10^{-7}	
	2.00×10^{-3}	1.20×10^{-7}	2.00
	1.00×10^{-3}	3.00×10^{-8}	2.00
	5.00×10^{-4}	7.51×10^{-9}	2.00
$P\text{-}ERK_{10,8,2}$	4.00×10^{-3}	3.83×10^{-7}	
	2.00×10^{-3}	9.59×10^{-8}	2.00
	1.00×10^{-3}	2.39×10^{-8}	2.00
	5.00×10^{-4}	6.00×10^{-9}	2.00
$P\text{-}ERK_{10,9,2}$	4.00×10^{-3}	3.13×10^{-7}	
	2.00×10^{-3}	7.83×10^{-8}	2.00
	1.00×10^{-3}	1.95×10^{-8}	2.00
	5.00×10^{-4}	4.90×10^{-9}	2.00
$P\text{-}ERK_{10,10,2}$	4.00×10^{-3}	2.61×10^{-7}	
	2.00×10^{-3}	6.53×10^{-8}	2.00
	1.00×10^{-3}	1.63×10^{-8}	2.00
	5.00×10^{-4}	4.09×10^{-9}	2.00
Random	1.00×10^{-3}	9.27×10^{-8}	
	5.00×10^{-4}	2.31×10^{-8}	2.00
	2.50×10^{-4}	5.78×10^{-9}	2.00
	1.25×10^{-4}	1.49×10^{-9}	1.95

variation in the span-wise direction [45]. Previous studies have demonstrated that a laminar separation bubble forms on the suction side of the airfoil and an unsteady wake propagates downstream.

Since the flow is fundamentally planar, we use a two-dimensional mesh of size $[-80, 100] \times [-80, 80]$ as shown in Figure 6a, which is as large as those used in previous studies [45]. The quadratically curved mesh is composed of 18,698 quadrilateral elements. The mesh is refined in the wake region to capture the unsteady flow downstream of the airfoil. The mesh is also refined towards the surface of the airfoil and thin boundary layer elements are used to capture the near-wall viscous features of the flow as shown in Figure 6b. The solution is represented using Gauss points on each element and the interface fluxes are computed using a Rusanov flux and the second method of Bassi and Rebay (BR2) with Gauss points along each element edge [47]. The surface of the airfoil is modelled as no-slip adiabatic, and the far field boundary condition is specified as Riemann invariant.

To assess the performance of the new family of RK schemes we compare them to the commonly used classical $\text{RK}_{3,3}$ scheme using solution polynomials of degree $k = 1$ to $k = 4$. This is the range of polynomial degrees for which that majority of practical simulations using FR and DG are performed [45, 48, 49]. We choose to compare against $\text{RK}_{3,3}$ since the classical $\text{RK}_{2,2}$ is not commonly used in practice, due to its aforementioned poor stability properties when using high polynomial degrees for the spatial discretization. We first determine the maximum stable time-step size iteratively for each polynomial degree with $\text{RK}_{3,3}$, and compute its corresponding computational cost as wall clock time per t_c, where $t_c = c/U_\infty$ is a non-dimensional convective time. We then find the maximum stable time-step size using the optimal $\text{P-ERK}_{16,16,2}$ scheme in the entire domain for each polynomial degree. We then split the domain into successive regions of stiffness based on each elements minimum edge length such that the maximum stable time step size is not reduced. $\text{P-ERK}_{16,16,2}$ is used in the stiffest part and, as the minimum element edge length increases, we use $\text{P-ERK}_{16,12,2}$, $\text{P-ERK}_{16,8,2}$, $\text{P-ERK}_{16,4,2}$, $\text{P-ERK}_{16,3,2}$, and finally $\text{P-ERK}_{16,2,2}$ for the largest elements in the domain. Using this approach we are able to use the same maximum time-step size as $\text{P-ERK}_{16,16,2}$ when it is used in the entire domain, but require significantly fewer stage derivative evaluations for the majority of elements. The splitting between P-ERK schemes is provided in Figure 7 showing that schemes with a large number of derivative evaluations are used for the small boundary layer elements, whereas fewer derivative evaluations are required moving outwards from the airfoil surface. Finally, each simulation is run to a final simulation time of $100t_c$ with a time-step 75% the size of the maximum found using the $\text{RK}_{3,3}$ and $\text{P-ERK}_{16,16,2}$ schemes, respectively.

The ratios of the maximum stable time step size achieved using P-ERK schemes relative to the $\text{RK}_{3,3}$ scheme are shown in Table 2 for each polynomial degree. We find that $\text{P-ERK}_{16,e,2}$ schemes can remain stable while taking time steps up to 6.07 times larger than $\text{RK}_{3,3}$. This increased time step size comes at the relatively small cost of additional derivative evaluations for a small number of stiff elements in the boundary layer region, as shown in Figure 7. As a result, we observe speedup factors of up to 4.98 relative to $\text{RK}_{3,3}$. This demonstrates that these new P-ERK schemes can significantly accelerate solutions of locally stiff systems of equations. Contours of vorticity shown in Figure 8 demonstrate that the P-ERK schemes remain stable, regardless of the solution polynomial degree. Furthermore, there is no apparent contamination of the solution at the interface between schemes. We observe that high-order solution polynomials better resolve the unsteady wake behind the aerofoil. Quantitative results including time-averaged lift ($\overline{C_L}$) and drag ($\overline{C_D}$) coefficients given in Table 2 are in excellent agreement with available reference data [45, 46]. Importantly, we note that results obtained using the P-ERK schemes are nearly identical to those obtained using $\text{RK}_{3,3}$, suggesting that the observed speedup factors are obtained without a significant impact on the accuracy. These results demonstrate that P-ERK schemes are a stable and efficient time stepping approach for unsteady simulations using the Navier-Stokes equations. Furthermore, they can be combined based on local numerical stiffness to achieve significant speedup factors compared to conventional approaches, while maintaining stability and accuracy.

5.3 Turbulent SD7003 Airfoil

To demonstrate the utility of P-ERK schemes for Implicit Large Eddy Simulation (ILES) using the Navier-Stokes equations at higher Reynolds numbers we consider transitional and turbulent flow over an SD7003

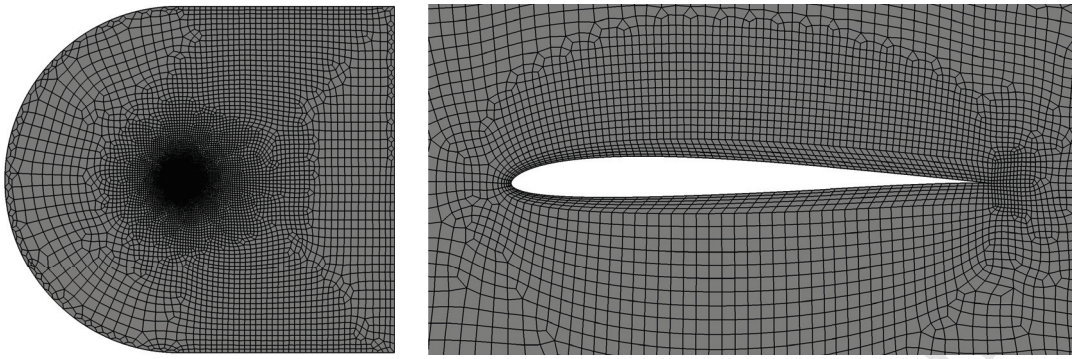

(a) Domain and mesh. (b) Near-surface mesh.

Figure 6. The domain and near surface meshes for the laminar SD7003 airfoil simulations showing the refined boundary layer region.

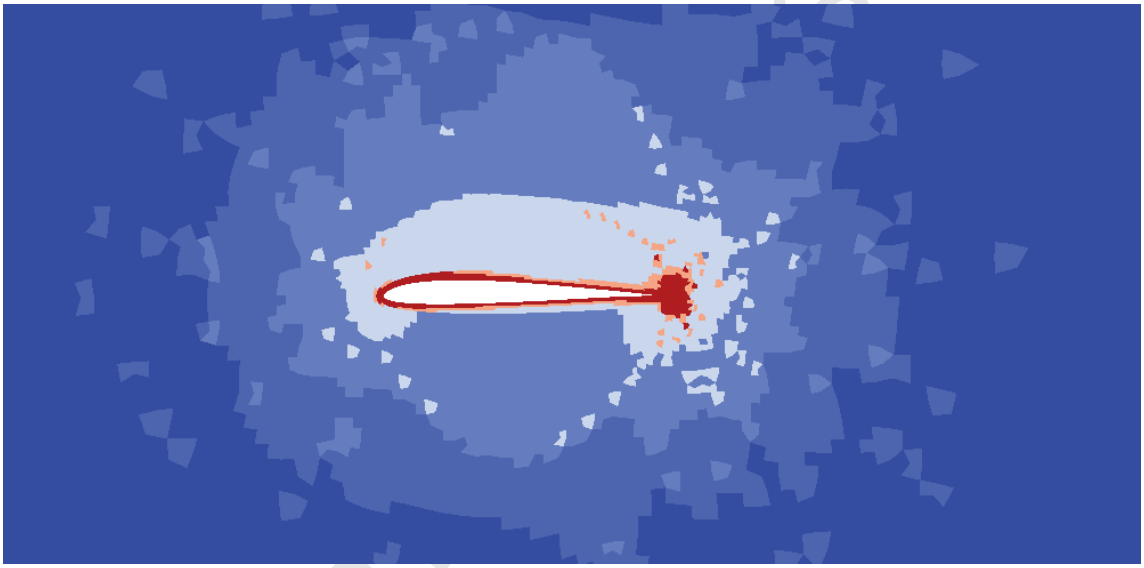

Figure 7. Splitting of the domain for the laminar SD7003 airfoil simulations into regions where P-ERK$_{16,16,2}$ (red), P-ERK$_{16,12,2}$, P-ERK$_{16,8,2}$, P-ERK$_{16,4,2}$, P-ERK$_{16,3,2}$, and P-ERK$_{16,2,2}$ (dark blue) are used based on minimum element edge lengths.

Table 2. Performance and quantitative results for the SD7003 airfoil test case.

Polynomial Degree	Scheme	Δt Ratio	Speedup Factor	$\overline{C_L}$	$\overline{C_D}$
$k = 1$	RK$_{3,3}$			0.3162	0.0516
	P-ERK$_{16,e,2}$	5.85	4.98	0.3163	0.0516
$k = 2$	RK$_{3,3}$			0.3893	0.0497
	P-ERK$_{16,e,2}$	5.84	4.24	0.3894	0.0497
$k = 3$	RK$_{3,3}$			0.3841	0.0499
	P-ERK$_{16,e,2}$	6.07	4.33	0.3841	0.0499
$k = 4$	RK$_{3,3}$			0.3849	0.0499
	P-ERK$_{16,e,2}$	5.76	3.41	0.3848	0.0499
Uranga et al. [45]				0.3755	0.0498
Lopez-Morales et al. [46]				0.3719	0.0494

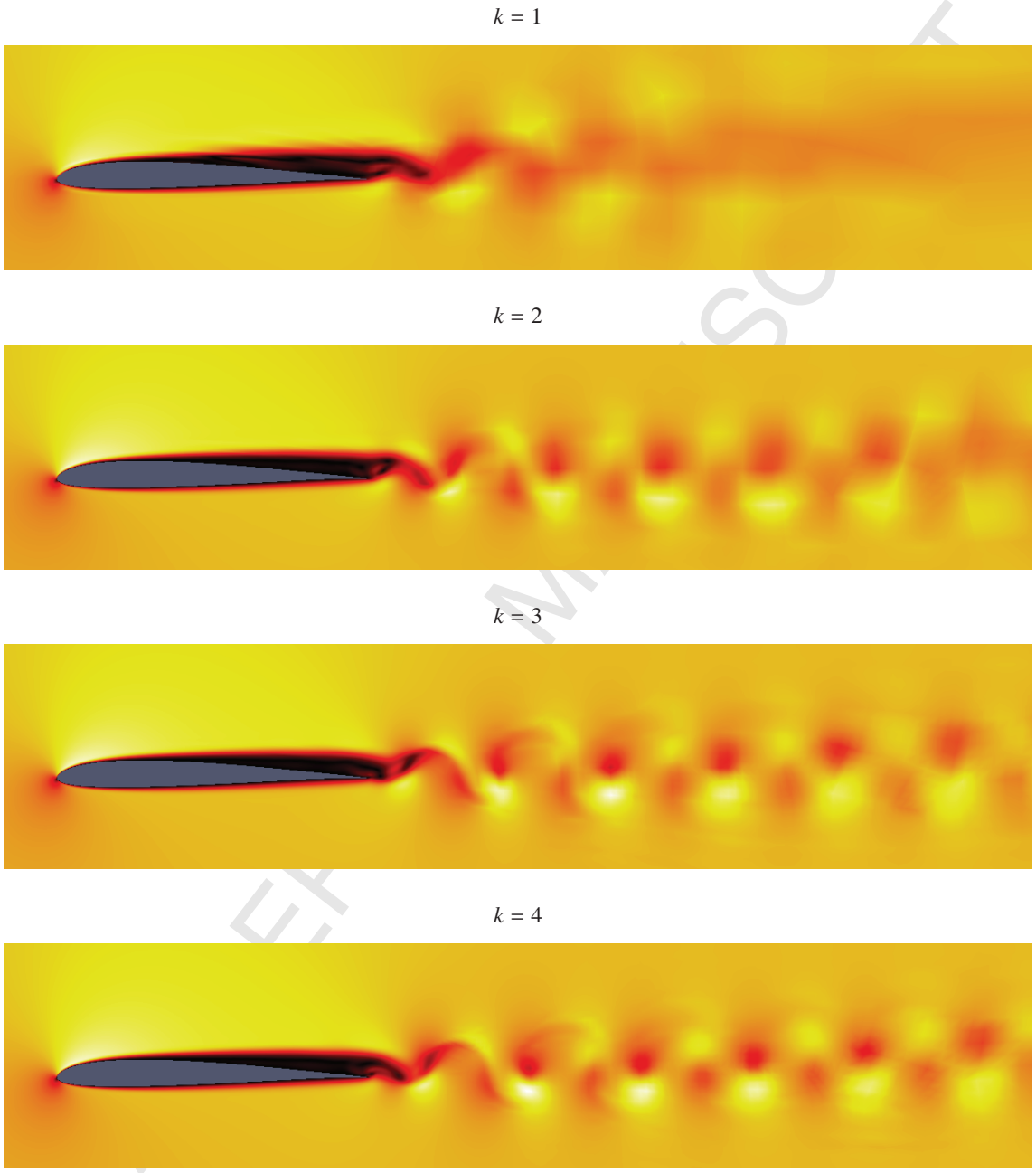

Figure 8. Coloured contours of velocity magnitude for the laminar SD7003 airfoil test cases.

airfoil. We use a freestream Mach number of $M = 0.1$, angle of attack $\alpha = 8°$, ratio of specific heats $\gamma = 1.4$, Prandtl number $Pr = 0.71$, and Reynolds number $Re_c = 60,000$. This is a commonly used test case for validation of LES solvers and multiple reference datasets are available for comparison [48, 50, 51]. At this Reynolds number and angle of attack a laminar separation bubble is expected to occur on the suction side of the airfoil, with turbulent transition occurring partway along its length.

Since the flow is turbulent we use a three-dimensional mesh of size $[-19, 20] \times [-20, 20] \times [0, 0.2]$ as shown in Figure 9a, which is as large as those used in similar previous studies [45]. The quadratically curved mesh is composed of 76,464 hexahedral elements with six elements in the spanwise direction. The mesh is refined in the wake region to capture the unsteady flow downstream of the airfoil. The mesh is also refined towards the surface of the airfoil and thin boundary layer elements are used to capture the near-wall viscous features of the flow, as shown in Figure 9b. Due to the relatively high Reynolds number, these elements are significantly thinner than those in the laminar SD7003 test case. The solution is represented using Gauss points on each element and the interface fluxes are computed using the Rusanov and BR2 schemes using Gauss points along each element face. The surface of the airfoil is modelled as no-slip adiabatic, and the far field boundary condition is specified as Riemann invariant.

Similar to the laminar SD7003 case, we first determined the maximum stable time-step size iteratively using both $RK_{3,3}$ and P-$ERK_{16,16,2}$, and the computational cost as wall clock time per convective time. This was performed for solution polynomials of degree $k = 1$, $k = 2$, and $k = 3$, for which ILES has previously been validated using the FR approach [49]. The boundary layer resolution gives $y^+ \approx 0.77$, 0.41, and 0.25 for solution polynomials of degree $k = 1$, 2, and 3, respectively, where $y^+ = u_\tau y/\nu$, y is the wall normal distance to the first solution point, ν is the kinematic viscosity, $u_\tau = \sqrt{C_f/2U_\infty}$, and $C_f \approx 8.5 \times 10^{-3}$ is the maximum skin friction coefficient in the turbulent region reported by Garmann et al. [51]. We then split the domain into P-$ERK_{16,16,2}$, P-$ERK_{16,12,2}$, P-$ERK_{16,8,2}$, P-$ERK_{16,4,2}$, P-$ERK_{16,3,2}$, and P-$ERK_{16,2,2}$ regions based on the minimum element edge lengths, as shown in Figure 10. This shows that schemes with a high number of stage derivative evaluations are concentrated near the surface of the airfoil, where the discretization is numerically stiff due to the thin boundary layer elements. In contrast, schemes with fewer derivative evaluations are use in the wake and far field regions where the element size is relatively large. Results in Table 3 show that the P-ERK schemes are able to take time steps up to 6.87 times larger than $RK_{3,3}$, resulting in speedup factors of up to 4.60. This demonstrates that P-ERK schemes can significantly accelerate the solution of unsteady turbulent flows.

The P-ERK simulations were then run to a final solution time of $t = 40t_c$, and time-averaged statistics were collected starting at $t = 20t_c$ including the average lift coefficient, average drag coefficient, separation point x_{sep}, and reattachment point x_{rea} for all polynomial degrees. Contours of q-criterion coloured by velocity magnitude in Figure 11 show that the P-ERK schemes remain stable for all polynomial degrees, and are qualitatively consistent with previous studies [48, 50, 51]. Importantly, we do not observe any degradation of the solution at the interfaces between the different P-ERK schemes. At this angle of attack a small separation bubble is observed near the leading edge of the airfoil. The flow undergoes turbulent transition partway along this separation bubble, and a turbulent wake propagates downstream with the mean flow. Quantitative results provided in Table 3 demonstrate that $\overline{C_L}$, $\overline{C_D}$, x_{sep}/c, and x_{rea}/c converge to the reference values under p-refinement, with the $k = 3$ simulation showning good agreement with previous studies for all measured parameters. In addition, the time averaged pressure coefficient on the surface of the airfoil shows good agreement with the reference datasets for the $k = 3$ simulation, as shown in Figure 12. Hence, these results demonstrate the P-ERK schemes can be used for turbulent wall bounded flows, achieving speedup factors of up to 4.60 while maintaining excellent agreement with the reference datasets.

6 Conclusions

We have introduced a new family of Paired Explicit Runge-Kutta (P-ERK) schemes for the solution of stiff systems of equations. The general formulation of P-ERK schemes allows methods with a large number

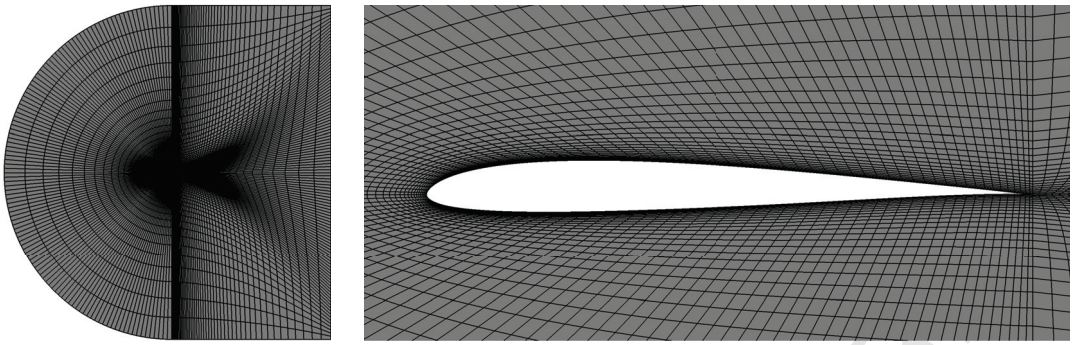

(a) Domain and mesh. (b) Near-surface mesh.

Figure 9. The domain and near surface meshes for the turbulent SD7003 airfoil simulations showing the refined boundary layer region.

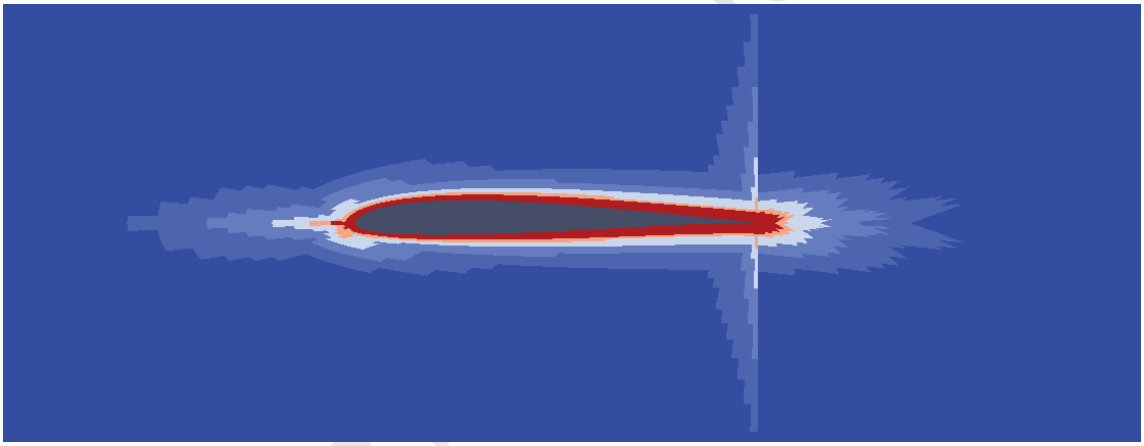

Figure 10. Splitting of the domain for the turbulent SD7003 airfoil simulations into regions where P-ERK$_{16,16,2}$ (red), P-ERK$_{16,12,2}$, P-ERK$_{16,8,2}$, P-ERK$_{16,4,2}$, P-ERK$_{16,3,2}$, and P-ERK$_{16,2,2}$ (dark blue) are used based on minimum element edge lengths.

Table 3. Performance and quantitative results for the SD7003 airfoil test case.

Polynomial Degree	Δt Ratio	Speedup Factor	$\overline{C_L}$	$\overline{C_D}$	x_{sep}/c	x_{rea}/c
$k = 1$	6.38	4.15	0.942	0.134	0.011	1.000
$k = 2$	6.87	4.60	0.959	0.042	0.035	0.277
$k = 3$	6.83	4.48	0.940	0.049	0.037	0.318
Garmann et al. [51]			0.969	0.039	0.023	0.259
Beck et al. [50]			0.932	0.050	0.030	0.336
Vermeire et al. [48]			0.941	0.049	0.045	0.315

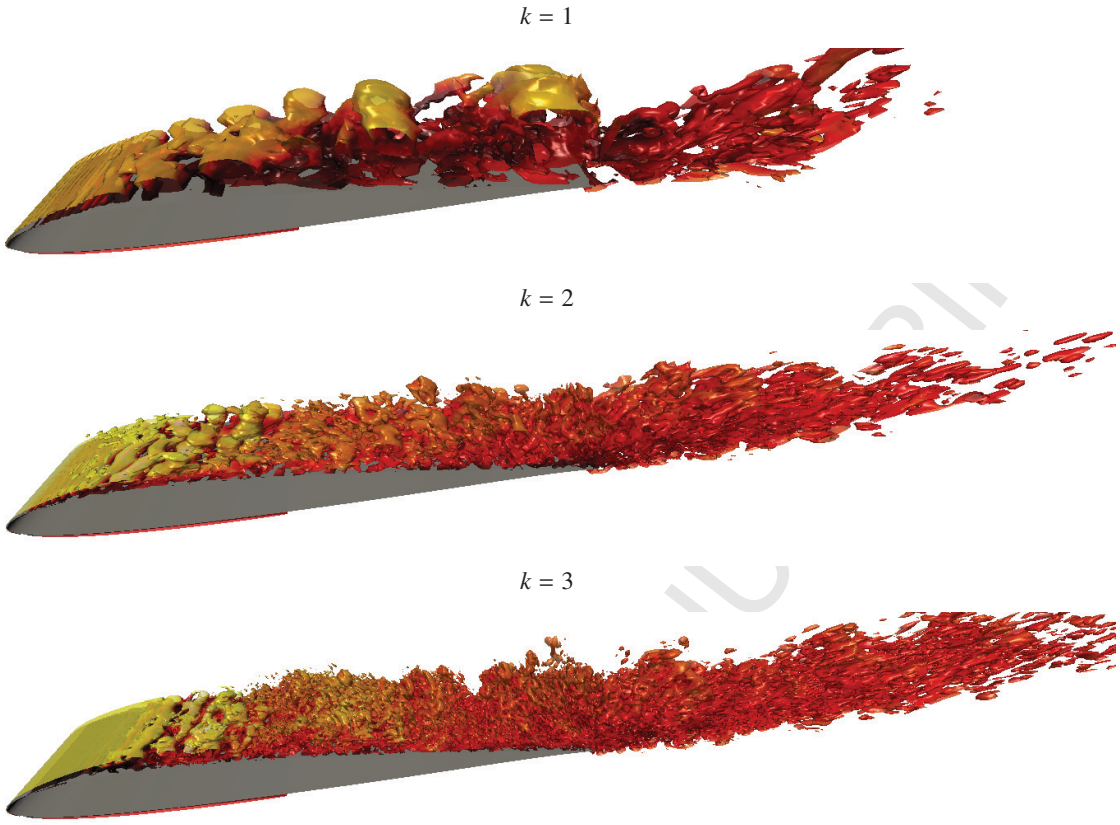

Figure 11. Contours of q-criterion coloured by velocity magnitude for the turbulent SD7003 airfoil test cases.

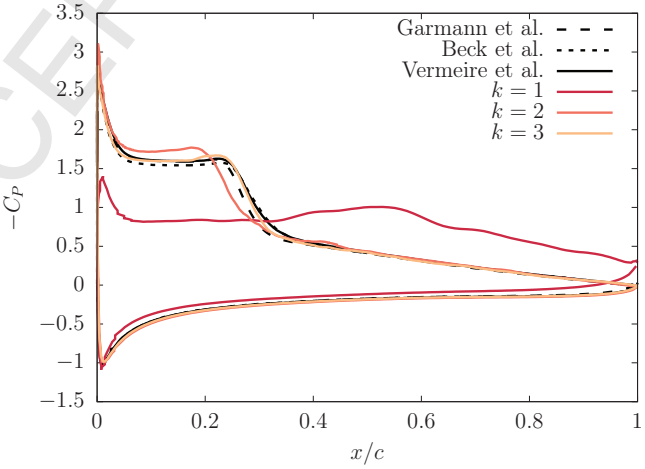

Figure 12. Plot of pressure coefficient distribution for the turbulent SD7003 airfoil.

of derivative evaluations and a large stability region to be used in the stiff parts of the domain, whereas methods with relatively few derivative evaluations are used in the non-stiff parts to reduce computational cost. Importantly, different methods with different numbers of derivative evaluations can be easily paired. Furthermore, the general stability polynomial of these P-ERK schemes allows them to be easily optimized for a given spatial discretization.

We then applied P-ERK schemes to solve the Euler equations and Navier-Stokes equations using a high-order unstructured FR spatial discretization. Results from an isentropic vortex test case demonstrated that P-ERK schemes with the same number of stages but different numbers of derivative evaluations can be paired in arbitrary combinations while still obtaining their designed second-order accuracy. Simulations using the Navier-Stokes equations demonstrated that significant speedup factors can be obtained relative to classical RK methods. In the case of an SD7003 airfoil speedup factors of up to 4.98 were observed for the laminar test case, while maintaining excellent agreement with reference data and identical simulations run using a classical $RK_{3,3}$ scheme. We then demonstrated that P-ERK schemes can be used for higher Reynolds number turbulent flow over an SD7003 airfoil. Again, significant speedup factors of up to 4.60 were observed while maintaining agreement with available reference datasets.

It has been demonstrated that P-ERK schemes allow significantly larger time steps to be taken relative to conventional explicit methods. Furthermore, by pairing several P-ERK schemes within a family, the number of stage derivative evaluations can be tuned to the local numerical stiffness, reducing overall computational cost. Future work will focus on generating higher-order P-ERK schemes and on their application to increasingly stiff systems of equations. Furthermore, we will explore extensions of this approach to systems of equations that have large negative real components, such as the diffusion equation or low-Reynolds number application of the Navier-Stokes equations, and adaptive time-stepping for when numerical stiffness is dependent on the local solution.

Acknowledgements

We acknowledge the support of the Natural Sciences and Engineering Research Council of Canada (NSERC), [RGPAS-2017-507988, RGPIN-2017-06773]. This research was enabled in part by support provided by Calcul Quebec (www.calculquebec.ca), WestGrid (www.westgrid.ca) and Compute Canada (www.computecanada.ca) via a Resources for Research Groups allocation.

Data Statement

Data relating to the results in this manuscript can be downloaded as Electronic Supplementary Material under a CC-BY-NC-ND 4.0 license.

References

[1] H.J. Stetter. *Analysis of discretization methods for ordinary differential equations*. Springer, 2 edition, 1973.

[2] E. Hairer, S. P. Nørsett, and G. Wanner. *Solving Ordinary Differential Equations I: Nonstiff Problems*. Springer Series in Computational Mathematics. Springer-Verlag, Berlin Heidelberg, 2 edition, 1993.

[3] E. Hairer and H. Wanner. *Solving Ordinary Differential Equations II - Stiff and Differential-Algebraic Problems*. Springer, 2 edition, 1996.

[4] U. M. Ascher, S. J. Ruuth, and R. J. Spiteri. Implicit-explicit Runge-Kutta methods for time-dependent partial differential equations. *Applied Numerical Mathematics*, 25(2–3):151–167, November 1997.

[5] M. Shoeybi, M. Svärd, F. E. Ham, and P. Moin. An adaptive implicit-explicit scheme for the DNS and LES of compressible flows on unstructured grids. *Journal of Computational Physics*, 229(17):5944–5965, August 2010.

[6] W. Hundsdorfer and J. Jaffré. Implicit-explicit time stepping with spatial discontinuous finite elements. *Applied Numerical Mathematics*, 45(2–3):231–254, 2003.

[7] A. Kanevsky, M. H. Carpenter, D. Gottlieb, and J. S. Hesthaven. Application of implicit-explicit high order Runge-Kutta methods to discontinuous-Galerkin schemes. *Journal of Computational Physics*, 225(2):1753–1781, August 2007.

[8] B. C. Vermeire and S. Nadarajah. Adaptive IMEX schemes for high-order unstructured methods. *Journal of Computational Physics*, 280:261–286, 2015.

[9] V. Allampalli, R. Hixon, M. Nallasamy, and S. D. Sawyer. High-accuracy large-step explicit Runge–Kutta (HALE-RK) schemes for computational aeroacoustics. *Journal of Computational Physics*, 228(10):3837–3850, June 2009.

[10] T. Toulorge and W. Desmet. Optimal Runge–Kutta schemes for discontinuous Galerkin space discretizations applied to wave propagation problems. *Journal of Computational Physics*, 231(4):2067–2091, February 2012.

[11] R. Diehl, K. Busch, and J. Niegemann. Comparison of Low-Storage Runge-Kutta Schemes for Discontinuous Galerkin Time-Domain Simulations of Maxwell's Equations. *Journal of Computational and Theoretical Nanoscience*, 7(8):1572–1580, August 2010.

[12] J. Niegemann, R. Diehl, and K. Busch. Efficient low-storage Runge–Kutta schemes with optimized stability regions. *Journal of Computational Physics*, 231(2):364–372, January 2012.

[13] M. Bernardini and S. Pirozzoli. A general strategy for the optimization of Runge–Kutta schemes for wave propagation phenomena. *Journal of Computational Physics*, 228(11):4182–4199, June 2009.

[14] M. Parsani, D. Ketcheson, and W. Deconinck. Optimized Explicit Runge–Kutta Schemes for the Spectral Difference Method Applied to Wave Propagation Problems. *SIAM Journal on Scientific Computing*, 35(2):A957–A986, January 2013.

[15] E. J. Kubatko, B. A. Yeager, and D. I. Ketcheson. Optimal Strong-Stability-Preserving Runge–Kutta Time Discretizations for Discontinuous Galerkin Methods. *Journal of Scientific Computing*, 60(2):313–344, August 2014.

[16] P. J. van Der Houwen and B. P. Sommeijer. On the internal stability of explicit, m-stage Runge-Kutta methods for large m-values. *ZAMM - Journal of Applied Mathematics and Mechanics / Zeitschrift für Angewandte Mathematik und Mechanik*, 60(10):479–485, 1980.

[17] A.A. Medovikov. High order explicit methods for parabolic equations. *BIT Numerical Mathematics*, 38(2):372, Jun 1998.

[18] A. Abdulle and A.A. Medovikov. Second order Chebyshev methods based on orthogonal polynomials. *Numerische Mathematik*, 90(1):1–18, Nov 2001.

[19] A. Abdulle. Fourth order Chebyshev methods with recurrence relation. *SIAM J. Sci. Comput.*, 23(6):2041–2054, June 2001.

[20] A. Abdulle and G. Vilmart. PIROCK: A swiss-knife partitioned implicit–explicit orthogonal Runge–Kutta Chebyshev integrator for stiff diffusion–advection–reaction problems with or without noise. *Journal of Computational Physics*, 242:869 – 888, 2013.

[21] J. Martín-Vaquero and B. Janssen. Second-order stabilized explicit Runge–Kutta methods for stiff problems. *Computer Physics Communications*, 180(10):1802 – 1810, 2009.

[22] S. O'Sullivan. A class of high-order Runge-Kutta-Chebyshev stability polynomials. *J. Comput. Phys.*, 300(C):665–678, November 2015.

[23] S. O'Sullivan. Factorized Runge-Kutta-Chebyshev methods. *Journal of Physics: Conference Series*, 837:012020, may 2017.

[24] S. O'Sullivan. Runge-Kutta-Gegenbauer methods for advection-diffusion problems, 2017.

[25] J. G. Verwer, B. P. Sommeijer, and W. Hundsdorfer. RKC time-stepping for advection-diffusion-reaction problems. *J. Comput. Phys.*, 201(1):61–79, November 2004.

[26] D. Ketcheson and A. Ahmadia. Optimal stability polynomials for numerical integration of initial value problems. *Communications in Applied Mathematics and Computational Science*, 7(2):247–271, 2012.

[27] E. M. Constantinescu and A. Sandu. Multirate Timestepping Methods for Hyperbolic Conservation Laws. *Journal of Scientific Computing*, 33(3):239–278, 2007.

[28] B. Seny, J. Lambrechts, R. Comblen, V. Legat, and J. F. Remacle. Multirate time stepping for accelerating explicit discontinuous Galerkin computations with application to geophysical flows. *International Journal for Numerical Methods in Fluids*, 71(1):41–64, 2012.

[29] M. Schlegel, O. Knoth, M. Arnold, and R. Wolke. Multirate Runge–Kutta schemes for advection equations. *Journal of Computational and Applied Mathematics*, 226(2):345–357, 2009.

[30] H. T. Huynh. A Flux Reconstruction Approach to High-Order Schemes Including Discontinuous Galerkin Methods. In *18th AIAA Computational Fluid Dynamics Conference*, volume AIAA 2007-4079. American Institute of Aeronautics and Astronautics, 2007.

[31] H. T. Huynh. A Reconstruction Approach to High-Order Schemes Including Discontinuous Galerkin for Diffusion. In *47th AIAA Aerospace Sciences Meeting including The New Horizons Forum and Aerospace Exposition*. American Institute of Aeronautics and Astronautics, January 2009.

[32] Matlab 2016a, 2016. The MathWorks, Natick, MA, USA.

[33] M. Grant and S. Boyd. CVX: Matlab software for disciplined convex programming, version 2.1. http://cvxr.com/cvx, March 2014.

[34] M. Grant and S. Boyd. Graph implementations for nonsmooth convex programs. In V. Blondel, S. Boyd, and H. Kimura, editors, *Recent Advances in Learning and Control*, Lecture Notes in Control and Information Sciences, pages 95–110. Springer-Verlag Limited, 2008. http://stanford.edu/~boyd/graph_dcp.html.

[35] W. H. Reed and T. R. Hill. Triangular mesh methods for the neutron transport equation. Technical Report LA-UR-73-479; CONF-730414-2, Los Alamos Scientific Lab., N.Mex. (USA), 1973.

[36] B. Cockburn and C. Shu. TVB Runge-Kutta local projection discontinuous Galerkin finite element method for conservation laws. II. General framework. *Mathematics of Computation*, 52(186):411–435, 1989.

[37] W. Liu, M. Vinokur, and Z. J. Wang. Spectral difference method for unstructured grids I: Basic formulation. *Journal of Computational Physics*, 216(2):780–801, 2006.

[38] Z. J. Wang, Y. Liu, G. May, and A. Jameson. Spectral Difference Method for Unstructured Grids II: Extension to the Euler Equations. *Journal of Scientific Computing*, 32(1):45–71, 2007.

[39] P. E. Vincent, P. Castonguay, and A. Jameson. Insights from von Neumann analysis of high-order flux reconstruction schemes. *Journal of Computational Physics*, 230(22):8134–8154, September 2011.

[40] B. C. Vermeire and P. E. Vincent. On the properties of energy stable flux reconstruction schemes for implicit large eddy simulation. *Journal of Computational Physics*, 327:368–388, 2016.

[41] B. C. Vermeire and P. E. Vincent. On the behaviour of fully-discrete flux reconstruction schemes. *Computer Methods in Applied Mechanics and Engineering*, 315:1053–1079, 2017.

[42] P. E. Vincent, P. Castonguay, and A. Jameson. A New Class of High-Order Energy Stable Flux Reconstruction Schemes. *Journal of Scientific Computing*, 47(1):50–72, April 2011.

[43] Z.J. Wang, K. Fidkowski, R. Abgrall, D. Caraeni, F. Bassi, A. Cary, H. Deconinck, R. Hartmann, K. Hillewaert, H. T. Huynh, N. Kroll, G. May, P. Persson, B. van Leer, and M. Visbal. High-order CFD methods: current status and perspective. *International Journal for Numerical Methods in Fluids*, 72(8):811–845, 2013.

[44] F. D. Witherden, A. M. Farrington, and P. E. Vincent. PyFR: An open source framework for solving advection–diffusion type problems on streaming architectures using the flux reconstruction approach. *Computer Physics Communications*, 185(11):3028–3040, 2014.

[45] A. Uranga, P. Persson, M. Drela, and J. Peraire. Implicit Large Eddy Simulation of transition to turbulence at low Reynolds numbers using a Discontinuous Galerkin method. *International Journal for Numerical Methods in Engineering*, 87(1-5):232–261, 2011.

[46] M. R. López, A. Sheshadri, J. R. Bull, T. D. Economon, J. Romero, J. E. Watkins, D. M. Williams, F. Palacios, A. Jameson, and D. E. Manosalvas. Verification and Validation of HiFiLES: a High-Order LES unstructured solver on multi-GPU platforms. In *32nd AIAA Applied Aerodynamics Conference*, number AIAA 2014-3168. American Institute of Aeronautics and Astronautics, 2014.

[47] F. Bassi and S. Rebay. A High-Order Accurate Discontinuous Finite Element Method for the Numerical Solution of the Compressible Navier-Stokes Equations. *Journal of Computational Physics*, 131(2):267–279, March 1997.

[48] B. C. Vermeire, F. D. Witherden, and P. E. Vincent. On the utility of GPU accelerated high-order methods for unsteady flow simulations: A comparison with industry-standard tools. *Journal of Computational Physics*, 334:497–521, 2017.

[49] B. C. Vermeire B. C., S. Nadarajah, and P. G. Tucker. Implicit large eddy simulation using the high-order correction procedure via reconstruction scheme. *International Journal for Numerical Methods in Fluids*, 82(5):231–260, 2015.

[50] Beck A. D., Bolemann T., Flad D., Frank H., Gassner G. J., Hindenlang F., and Munz C. D. High-order discontinuous Galerkin spectral element methods for transitional and turbulent flow simulations. *International Journal for Numerical Methods in Fluids*, 76(8):522–548, 2014.

[51] D. J. Garmann, M. R. Visbal, and P. D. Orkwis. Comparative study of implicit and subgrid-scale model large-eddy simulation techniques for low-Reynolds number airfoil applications. *International Journal for Numerical Methods in Fluids*, 71(12):1546–1565, 2013.